

# PHOTONICS Research

## High-efficiency and large light-receiving area superconducting nanowire single-photon detector integrated with high-contrast grating

CHEN WEI,<sup>1</sup>  WENCONG WANG,<sup>1</sup> DONGMEI LIU,<sup>1,2</sup>  MIN GU,<sup>1,3</sup> AND XIANQIU WU<sup>1</sup>

<sup>1</sup>School of Physics and Telecommunication Engineering, South China Normal University, Guangzhou 510006, China

<sup>2</sup>e-mail: dmliu@scnu.edu.cn

<sup>3</sup>e-mail: mingu@m.scnu.edu.cn

Received 5 August 2021; revised 15 September 2021; accepted 17 September 2021; posted 21 September 2021 (Doc. ID 439806); published 26 October 2021

By using a high-contrast grating (HCG, high transmittance >90%) to control the phase shift of incident light, we theoretically designed a novel-structured HCG-integrated superconducting nanowire single-photon detector (HCG-SNSPD) with a high-efficiency and large light-receiving area. Without enlarging the typical single-pixel SNSPD nanowire area ( $10\ \mu\text{m} \times 10\ \mu\text{m}$ ), the effective detection area is expanded to  $115\ \mu\text{m}$ , while the absorption efficiency of the nanowire reaches 84.9% at a wavelength of 1550 nm. The effective detection area of HCG-SNSPD is increased by 11.5 times compared to that of conventional single-pixel SNSPDs. Moreover, the absorption efficiencies of HCG-SNSPD exceed 70% at wavelengths ranging from 1460 nm to 1650 nm, indicating high-efficiency broadband detection. This study promotes new possibilities for the application of SNSPDs. © 2021 Chinese Laser Press

<https://doi.org/10.1364/PRJ.439806>

### 1. INTRODUCTION

Since Gol'tsman's first demonstration of the superconducting nanowire single-photon detector (SNSPD) [1] in 2001, it has undergone tremendous development [2–4]. Featuring high system detection efficiency [5–7], low dark count rate [8], short recovery time [9], and extremely low timing jitter [10], it has been used in a wide range of fields, such as quantum key distribution [11], laser ranging [12,13], space laser communication [14–16], and depth imaging [17]. However, compared with photomultiplier tubes or single-photon avalanche diodes (detection area from  $100\ \mu\text{m}$  to several millimeters in diameter), a typical single-pixel SNSPD detection area is usually only  $10\ \mu\text{m}$  in diameter [18], which limits the application of SNSPDs in certain scenarios, such as coupling with multimode fibers in deep space communications and lidar [19,20].

Increasing the effective detection area of the SNSPD is challenging. There are two main approaches to solving this problem. One of them is to increase the coverage area of the nanowires. Thus far, the maximum detection area of single-pixel SNSPDs with high efficiency is  $100\ \mu\text{m}$  in diameter, achieving a detection efficiency of 65% at 532 nm [21]. Another approach is to build SNSPD arrays to obtain a larger detection area by increasing the number of pixels. Few efficient large-area SNSPD arrays have been reported, such as a 16-pixel SNSPD with an effective area of  $80\ \mu\text{m} \times 80\ \mu\text{m}$ , achieving a

detection efficiency of 46% at 1064 nm [22], and a 64-pixel SNSPD with an effective area diameter of  $320\ \mu\text{m}$ , exhibiting a free-space system detection efficiency of 40% at 1550 nm [23]. Both these approaches have high requirements for the homogeneity of superconducting films and micro-nano processing. In addition, the former introduces a large kinetic inductance that results in a lower detection rate and longer recovery times. The latter requires a more complex readout circuit system [24].

In this study, we adopt a novel approach of integrating optical structures in SNSPDs to increase the effective detection area of the detector without enlarging the area of the nanowires. A high-contrast grating (HCG) optical structure [25], which is a subwavelength grating structure inscribed with a high-refractive-index difference, is used. Owing to its large refractive index difference and subwavelength size, HCG can provide high reflectivity or high transmissivity over a large bandwidth. Moreover, it possesses an interesting property: the ability to control the phase shift of reflected/transmitted light [26]. If the structural parameters of a grating, such as the period, duty cycle, and thickness, are changed, the phase shift of the reflected/transmitted light changes accordingly. This implies that we can control the phase shift of the light to focus on the reflected/transmitted side while maintaining a high reflectance/transmittance [27,28]. Shiono *et al.* points out that the reflected/transmitted light will be focused on a spot if the spatial distribution of the phase shift satisfies Eq. (1) [29]:

$$\phi(x) = -\frac{2\pi}{\lambda} \left( \sqrt{x^2 + f^2} - f \right) + \varphi_0, \quad (1)$$

where  $\lambda$  is the wavelength of the incident light in the propagating medium,  $f$  is the focal length,  $x$  is the distance from the grating center, and  $\varphi_0$  is the phase shift of the reflected/transmitted light at the position of the grating center.

In this study, we theoretically propose a design method that integrates HCG with focusing capability into SNSPD (HCG-SNSPD). The simulation results show that the transverse magnetic (TM)-polarized incident light at a wavelength of 1550 nm passes through the  $10 \mu\text{m} \times 115 \mu\text{m}$  HCG and forms a spot occupying 85.5% of the total energy in the  $10 \mu\text{m} \times 10 \mu\text{m}$  region in the middle of the focal plane. By placing nanowires at the spot location and using a cavity structure to improve absorption, we achieve a high efficiency of 84.9% of total incident light at 1550 nm. In other words, compared to that of conventional single-pixel SNSPDs, we have been able to expand the effective detection area to 11.5 times by integrating the structure of HCG with a single-pixel nanowire area of  $10 \mu\text{m} \times 10 \mu\text{m}$  and maintain a high absorption efficiency of 84.9%. Furthermore, the HCG-SNSPD has over 70% absorption efficiencies in the wavelength range of 1460–1650 nm, indicating a large high-efficiency bandwidth.

## 2. METHODS

A structural diagram of the HCG-SNSPD is shown in Fig. 1(a). HCG is located at the top of the structure. Si is selected as the grating material because of its high refractive index and its lack of absorption of incident light at 1550 nm. There is a vacuum gap between the gratings. Below the grating is a silicon dioxide ( $\text{SiO}_2$ ) dielectric layer, and light is transmitted in this medium after passing through the HCG. The  $\text{SiO}_2$  dielectric layer supports the HCG and does not absorb incident light. The function of HCG is similar to that of a light “funnel”: TM-polarized incident light is focused to the focal point. The gray dotted line in Fig. 1(a) indicates the focal path of the incident light. We placed nanowires made of niobium nitride (NbN) in a

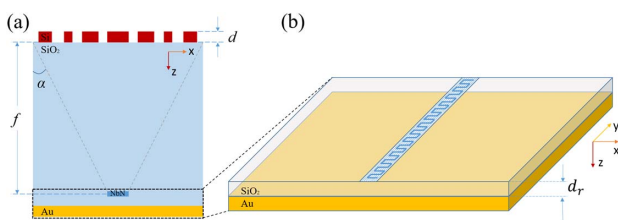


**Fig. 1.** (a) Schematic diagram of the structure of HCG-SNSPD. HCG is located at the top of the structure. It is made of a high-refractive-index material Si with a thickness of  $d$ . There is a vacuum gap between the gratings. The material of the layer below HCG is  $\text{SiO}_2$ . Incident light passes through HCG to focus on the  $\text{SiO}_2$  layer. The focal length is  $f$ . The NbN nanowire is located at the focal position, and there are several thick layers of  $\text{SiO}_2$  and an Au layer below the nanowires.  $\alpha$  is the angle between the gray dotted line (from the edge of the structure to the focal point) and the vertical direction. (b) Schematic diagram of the position of the nanowires, resonant cavity, and Au mirror at the bottom of the HCG-SNSPD. The shaded part indicates the focused bar, the meandering structures are the nanowires, and  $d_r$  is the thickness of the resonant cavity.

$10\text{-}\mu\text{m}$ -wide area at the focal position to facilitate the absorption of photons. An Au mirror was placed below the nanowires, and a layer of  $\text{SiO}_2$  was incorporated between them, forming an overall resonant cavity structure.

A detailed 3D schematic of the nanowires and resonant cavity below the structure is shown in Fig. 1(b). The shaded part above the  $\text{SiO}_2$  layer indicates the focused light bar. The meandering structures distributed in the shaded area are NbN nanowires. The nanowires cover an area of  $10 \mu\text{m} \times 10 \mu\text{m}$ , with a thickness of 8 nm, width of 100 nm, and filling factor of 0.5 (for the convenience of illustration, the figure is not drawn strictly to size scale). Below the nanowires, the resonant cavity formed by  $\text{SiO}_2$  and the Au mirror can cause unabsorbed photons to repeatedly pass through the nanowire area, thereby improving the absorption efficiency [30]. In our simulations, the refractive index of each material at 1550 nm is  $n_{\text{Si}} = 3.48$ ,  $n_{\text{SiO}_2} = 1.44$ ,  $n_{\text{NbN}} = 5.23 + 5.82i$ , and  $n_{\text{Au}} = 0.559 + 9.81i$ .

A schematic design of the HCG structure is shown in Fig. 2(a), which is divided into upper and lower parts. The upper part of Fig. 2(a) shows a 3D model of the HCG with TM-polarized light incident from the top, downwards along the  $z$  axis. During simulation, the length of the grating in the  $y$ -axis direction is taken to be infinite. To achieve the focusing effect, it is necessary to match the phase shift of the incident light at each position of the HCG, such that each grating

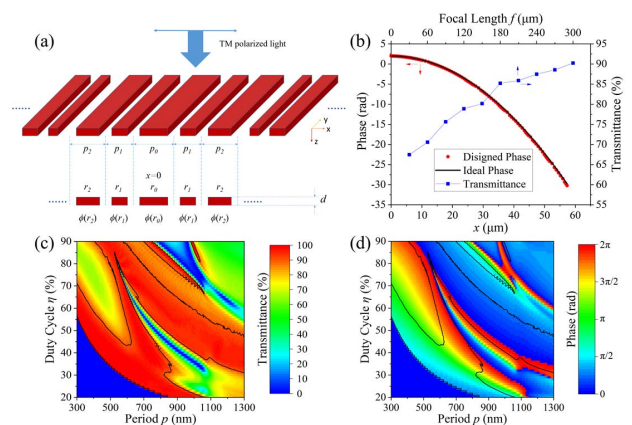


**Fig. 2.** (a) Schematic diagram of HCG design. The upper part is a 3D structural view of the grating. The TM-polarization plane wave is incident from the top, downwards toward the HCG. The lower part is the front view of the grating along the  $y$ -axis direction.  $p_n$  and  $r_n$  are the width and center position of each grating bar, respectively, and  $\phi(r_n)$  is the phase shift that should be satisfied when focusing. The position of  $r_0$  is defined as the origin of the  $x$  axis. (b) Comparison of the phase shifts corresponding to the grating parameters selected for the design with the ideal phase shift curve. The discrete red dots are the selected phase, and the solid black line is the ideal phase, corresponding to the left and lower axes. The value of  $x$  corresponding to each red dot represents the position of each grating bar  $r_n$  on the  $x$  axis. The blue square line is the design focal length versus transmittance, corresponding to the right and upper axes. (c) Transmittance table and (d) phase shift table of incident light passing through the HCG with thickness  $d = 0.75 \mu\text{m}$ . Areas with transmittance greater than 90% are surrounded by the solid line in both figures. Considering processing difficulty, aspect ratios of the parameters in the lower-left corner are too small to be included as candidates, and they are shown as zero value.

bar has a different width  $p$  (including bar-width  $w_g$  and gap). In addition, according to Eq. (1), the grating is symmetric around the central grating bar along the  $x$  axis. The lower part of Fig. 2(a) shows the front view of the HCG along the  $y$  axis, where  $r_n$  indicates the center of each grating bar. The grating bar at the center is considered as  $r_0$ , and this point is the origin of the  $x$  axis,  $r_0 = 0$ . Because of the symmetry of the grating, the left and right grating bars have the same structure; therefore, focusing only on one side would suffice.  $r_n$  indicates the  $n$ th grating bar on both sides when  $n > 0$ .  $\phi(r_n)$  represents the phase shift caused by each grating bar to the incident light. The value of  $\phi(r_n)$  and transmittance are controlled by the grating bar width  $p$  and the duty cycle  $\eta$  (the ratio of bar-width  $w_g$  and  $p$ ), when the grating thickness  $d$  is taken to be a fixed value. Moreover, according to the analysis in Ref. [31], the phase shift and transmittance caused by an individual grating unit in the nonperiodic grating are decided by the corresponding periodic grating with the same TM-polarized incident light.

To design a focused HCG, it is necessary to obtain the ideal phase shift distribution [the black curve in Fig. 2(b) of the transmitted light according to Eq. (1)]. Thereafter, we select the grating parameters that satisfy this phase shift distribution according to each spatial position. To achieve effective focus while ensuring a high transmittance, each grating bar is required to have high transmittance ( $>90\%$ ) to the incident light, and the phase shifts must cover the complete range from zero to  $2\pi$  (when the phase shift is less than zero or greater than  $2\pi$ , it is replaced with an equivalent value between zero and  $2\pi$ ). In this manner, the precise matching of the phase shift can be satisfied to achieve an improved focusing effect. To obtain transmittance and phase shift corresponding to gratings with different values of  $p$  and  $\eta$ , it is necessary to scan and calculate each value under periodic conditions to obtain the parameter candidate table.

Considering processing difficulty, the thickness of the gratings is chosen as  $0.75 \mu\text{m}$ . According to our calculations, a thickness greater than or less than  $0.75 \mu\text{m}$  will cause the phase shift table controlled by parameters  $p$  and  $\eta$  not to completely cover the complete range from zero to  $2\pi$  with transmittance greater than  $90\%$ , which reduces the transmittance and focus quality. In addition, to reduce the processing difficulty, we exclude the parameters with a grating aspect ratio less than  $1/5$  from the candidate range of the parameters [the near-triangular area in the lower-left corner of Figs. 2(c) and 2(d); the value of this area is shown as zero].

Figures 2(c) and 2(d) show the data tables of transmittance and phase shift corresponding to each  $p$  and  $\eta$ . In the calculated range of  $300 \text{ nm} < p < 1300 \text{ nm}$  and  $20\% < \eta < 90\%$ , a large high-transmittance region is shown in Fig. 2(c), where the area surrounded by solid lines indicates the region with a transmittance greater than  $90\%$ . This region is also marked in the phase shift table in Fig. 2(d), and the surrounding part covers the range from zero to  $2\pi$ , which can be considered as a complete phase shift candidate table.

To investigate the relationship between the focal length and transmittance of the corresponding focal plane [blue square line in Fig. 2(b)], we designed a few sets of HCGs with the same number of grating bars ( $r_0$ – $r_{99}$ , 199 grating bars in total).

The overall widths of all the sets of HCGs were approximately  $120 \mu\text{m}$ , and the focal lengths  $f$  were designed from  $30 \mu\text{m}$  to  $300 \mu\text{m}$ . The incident light was a TM-polarized plane wave with a wavelength of  $1550 \text{ nm}$ . In general, as the focal length increases, the transmittance of the corresponding focal plane also tends to increase. The transmittance at the focal plane reaches  $91.0\%$  at  $f = 300 \mu\text{m}$ . Considering that the conventional thickness of the  $\text{SiO}_2$  substrate, to be ensured for the manufacturing of devices in the future, is  $300 \mu\text{m}$ , micro–nano processing can be performed on both the front and back sides of the substrate via the double-sided scribing method, which affords higher transmittance, reducing the reflection loss and simplifying the device processing procedure. We chose this set of HCG parameters for a larger focal length  $f = 300 \mu\text{m}$ , where total width of the grating was  $115 \mu\text{m}$ .

The red discrete dots in Fig. 2(b) are the phase shifts corresponding to each grating bar in our design for HCG with  $f = 300 \mu\text{m}$ . Because each grating bar has several widths, the phase shifts are discrete distributions. The curve corresponding to our design is in good agreement with the ideal phase shift curve of Eq. (1). If the span between the phase shifts provided by the central grating bar and the outermost grating bar is greater than  $8\pi$  [ $\Delta\phi = \phi(r_{n_{\text{max}}}) - \phi(r_0) > 8\pi$ ], the incident light would form a focal point with a narrow width. The larger  $\Delta\phi$  is, the narrower the focal point width would be until it is close to the diffraction limit. In our designed parameters,  $\Delta\phi = \phi(r_{99}) - \phi(r_0) \approx 10.25\pi$ .

Figure 3(a) shows the cross-sectional normalized energy distribution; the HCG is at the top position at  $z = 0$ . It can be clearly seen that the light gradually converges after passing through the grating and forms a distinct focal point at a position approximately  $300 \mu\text{m}$  from the grating. The red curves in Fig. 3(b) indicate the normalized energy distribution at various locations along the line  $x = 0$ . The maximum value of the

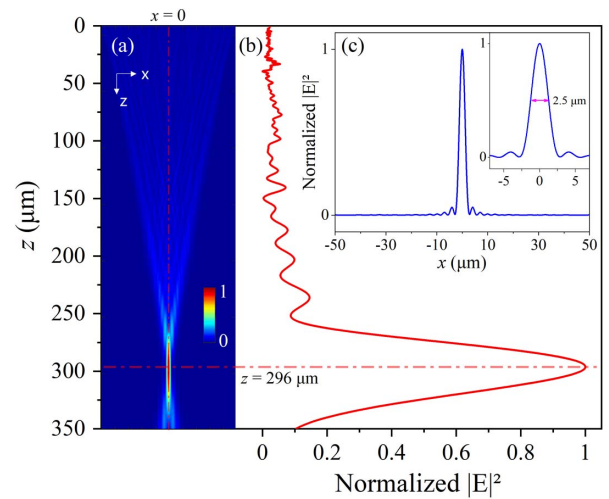


**Fig. 3.** Simulation results of the designed HCG with  $f = 300 \mu\text{m}$ . (a) Normalized energy field distribution of the cross section of the HCG. The actual focal point appears at  $296 \mu\text{m}$  from the grating. (b) Normalized energy distribution curves along the line  $x = 0$  (red curve). (c) Normalized energy distribution curves along the line  $z = 296 \mu\text{m}$  (blue curve). The inset shows a magnified view of the  $-5 \mu\text{m} < x < 5 \mu\text{m}$  region with an FWHM of  $2.5 \mu\text{m}$ .

normalized energy curve corresponds to  $z = 296 \mu\text{m}$ , which is the actual focal point position, and it matches the focal length of  $300 \mu\text{m}$  in our design. This small deviation can be attributed to the fact that the HCG can facilitate only the discrete control of phase shifts, but not particularly continuous per se, as shown in Eq. (1). The blue curve in Fig. 3(c) shows the normalized energy distribution at various locations along the line  $z = 296 \mu\text{m}$ , and the details of  $-5 \mu\text{m} < x < 5 \mu\text{m}$  are shown in the inset. Almost all the energy is concentrated in the region within approximately  $10 \mu\text{m}$  from the center, the full width at half maximum (FWHM) at the focal point is only approximately  $2.5 \mu\text{m}$ , and the side lobes are less than  $1/16$  of the intensity of the main peak. All of the above indicate that the designed HCG with  $f = 300 \mu\text{m}$  has a satisfactory focusing performance.

Additionally, the HCG also has a high transmittance of incident light. Figure 4(a) shows the transmittance spectra of the entire focal plane ( $-57.5 \mu\text{m} < x < 57.5 \mu\text{m}$ , red solid line), the  $30\text{-}\mu\text{m}$  central width region ( $-15 \mu\text{m} < x < 15 \mu\text{m}$ , blue solid line), and the  $10\text{-}\mu\text{m}$  central width region ( $-5 \mu\text{m} < x < 5 \mu\text{m}$ , green solid line). The maximum values of all three transmittance curves occur at  $1550 \text{ nm}$ , which is in line with our design expectations. As the wavelength increases from  $1550 \text{ nm}$ , each curve starts to decrease. However, the incident light at  $1550 \text{ nm}$  still has a high transmittance of  $91.0\%$ , even at a focal plane as far as  $296 \mu\text{m}$  from the grating. Transmittance values of  $88.6\%$  and  $85.6\%$  are achieved in the region of  $30\text{-}\mu\text{m}$  and  $10\text{-}\mu\text{m}$  widths at the center of the focal plane, respectively. This implies that nearly  $94.1\%$  of the incident light in the entire focal plane is concentrated in a central area with a width of only  $10 \mu\text{m}$ . It can also be found that the transmittance of HCG is above  $70\%$  at wavelengths from  $1460 \text{ nm}$  to  $1650 \text{ nm}$ , implying that it has a wide high-transmission bandwidth.

So far, we have verified the satisfactory focusing property and transmission effect of HCG that promises a possibility of the efficient absorption of incident light from a large area to a small area of nanowires. However, a new problem is encountered here: HCG causes a deflection of the vertical incident light. If the nanowires are placed at the focal point, the angle between the incident light and the nanowires is no longer  $90^\circ$ . To investigate the effect of this factor on absorption, we

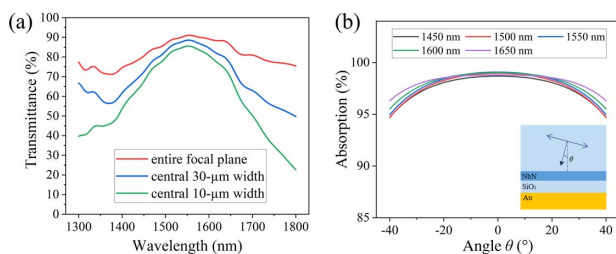


**Fig. 4.** (a) Transmittance spectrum at the focal plane. The red, blue, and green solid lines indicate the transmittance across the focal plane, the central  $30\text{-}\mu\text{m}$  width, and the central  $10\text{-}\mu\text{m}$  width, respectively. (b) Absorption of nanowire as a function of  $\theta$  of the incident light from  $1450 \text{ nm}$  to  $1650 \text{ nm}$ . The inset shows a schematic of the simulated structure, and  $\theta$  is defined as the angle between the incident direction and the vertical direction.

attempted to illuminate the nanowires with plane waves at different incident angles and obtain the absorption versus incident angle [Fig. 4(b)]. The inset shows the simulated structure. The source was placed in the  $\text{SiO}_2$  medium, and the polarization was parallel to the nanowire; the angle between the incident direction and the vertical direction is defined as  $\theta$ . The thickness and width of the nanowire were  $8 \text{ nm}$  and  $100 \text{ nm}$ , respectively, with a filling factor of  $50\%$ , and the thickness of the  $\text{SiO}_2$  layer below was  $265 \text{ nm}$ , with an Au mirror at the bottom. The results show that the absorption has a maximum value of  $99\%$  at  $\theta = 0^\circ$  in the range of  $0^\circ$  to  $\pm 40^\circ$ . For the wavelength range of  $1450\text{--}1650 \text{ nm}$ , the absorptions corresponding to each curve in the range of  $0^\circ$  to  $\pm 20^\circ$  almost overlap. As  $\theta$  gradually increases, the absorption gradually decreases, and the slope corresponding to the absorption decrease tends to increase gradually. However, even if  $\theta = \pm 40^\circ$ , the absorption of nanowires in this wavelength range has a high value close to  $95\%$ , which further proves the characteristics of broadband operation. The distance between the outermost side of the HCG and the center of our design is  $r_{99} = 57.5 \mu\text{m}$ , and the focal length  $f = 296 \mu\text{m}$ . It can be calculated that  $\alpha \approx 10.99^\circ$  in Fig. 1(a); that is, after the incident light is deflected by the HCG, the maximum value of the deflection angle is  $\pm 10.99^\circ$ , and the light incident at this angle can still achieve  $98.9\%$  absorption. Therefore, it can be considered that the angle deflection caused by the HCG to the incident light in this design does not have a significant impact on the absorption, and it features a large redundancy.

### 3. RESULTS AND ANALYSIS

We integrated the HCG with the SNSPD as shown in Fig. 1(a) and placed the nanowires at the focal point. The absorption efficiency of the detector (without the Au mirror) as a function of wavelength is indicated with blue dots in Fig. 5(a). In the range of  $1480\text{--}1640 \text{ nm}$ , the detector achieves an absorption efficiency of more than  $30\%$  with a peak absorption of  $33.53\%$  at  $1540 \text{ nm}$ . It is an appropriate absorption efficiency without auxiliary structures, but it is still not sufficient for practical applications. Therefore, we insert an optical resonant cavity

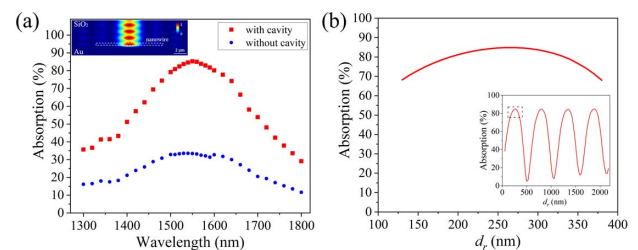


**Fig. 5.** (a) Absorption spectrum of HCG-SNSPD. The red squares and blue dots indicate the absorption with and without cavity structure, respectively. The inset shows the normalized energy field distribution results for the nanowire integrated with the cavity at the wavelength of  $1550 \text{ nm}$ . The widths of the field area in the horizontal and vertical directions are  $18 \mu\text{m}$  and  $4 \mu\text{m}$ , respectively. The nanowires are located in the dotted rectangle. (b) Absorption efficiency as a function of resonant cavity thickness ( $130 \text{ nm} < d_r < 380 \text{ nm}$ , the region in the dotted box in the inset). The inset shows the absorption curve at a wider variety of thickness ( $50 \text{ nm} < d_r < 2170 \text{ nm}$ ).

structure of metal–insulator nanowires underneath the nanowires to improve the absorption efficiency of the detector. The structure of the resonant cavity is described in the description of Fig. 1(b). We explored the relationship between the cavity thickness  $d_r$  and absorption efficiency, as shown in Fig. 5(b), with the wavelength of incident light equal to 1550 nm. The inset shows that the absorption has a periodic correspondence with  $d_r$ , when the thickness varies over a wide range. This illustrates that the cavity thickness  $d_r$  plays an extremely important role in enhancing the absorption efficiency, and a suitable thickness can significantly enhance the absorption, while an unsuitable thickness can suppress the absorption to less than 5%. We chose the thinnest cycle among them and considered the maximum absorption thickness in this cycle. As shown in Fig. 5(b), the nanowires have maximum absorption at  $d_r = 265$  nm, which is approximately 84.9%. This implies that we achieved an 84.9% absorption efficiency of  $115 \mu\text{m} \times 10 \mu\text{m}$  incident light by using nanowires with an area of  $10 \mu\text{m} \times 10 \mu\text{m}$ . The designed HCG-SNSPD affords an appropriate absorption efficiency for 11.5 times the incident area of the nanowires. Compared to Ref. [32] based on a dual-lens system employed for the compression of the beam size that achieved a system efficiency of 55% at 1550 nm, our design is more advantageous in terms of absorption efficiency. We analyzed the causes of loss of light, part of which is attributed to the reflection of incident light by the HCG (approximately 5.9%); part of the transmitted light fails to reach the focal point and is scattered to the sides of the device (approximately 5.6%). In addition, the cavity structure cannot make nanowires fully absorb the remaining photons (approximately 3.6%).

After obtaining the optical cavity thickness  $d_r = 265$  nm, we also calculated the absorption spectrum of the HCG-SNSPD in the wavelength range of 1300–1800 nm. As shown by the red squares in Fig. 5(a), the absorption efficiency is increased by more than two times, compared with the case without a cavity structure. The maximum absorption of 84.9% occurs at 1550 nm. For an incident light of 1500–1600 nm, the detector has an absorption above 80%, and for incident light of 1460–1650 nm, it still has a high absorption above 70%. This shows that the detector has a large high-absorption bandwidth, which might prove advantageous in various application scenarios. The inset in Fig. 5(a) shows the normalized energy field distribution around the nanowire at 1550 nm (with cavity). The incident light is basically absorbed when it is focused on the nanowires, because the gold layer and the cavity at the bottom cause the energy to be mainly concentrated in the central region of the nanowire. The width of the focused spot of the energy field is significantly smaller than that of the nanowire area, which provides a sufficient amount of redundancy for alignment between the top grating layer and the SNSPD active area layer.

In addition, we investigated the influence of the filling factor of the nanowires on the absorption. The thickness of the resonant cavity was considered as  $d_r = 265$  nm, and the incident light was 1550 nm. Figure 6 shows the relationship between the filling factor and the absorption. The definition of the filling factor is shown in the inset, that is, the ratio of the nanowire width  $w_{\text{NBW}}$  to the pitch  $w_p$ . As shown in Fig. 6, when the

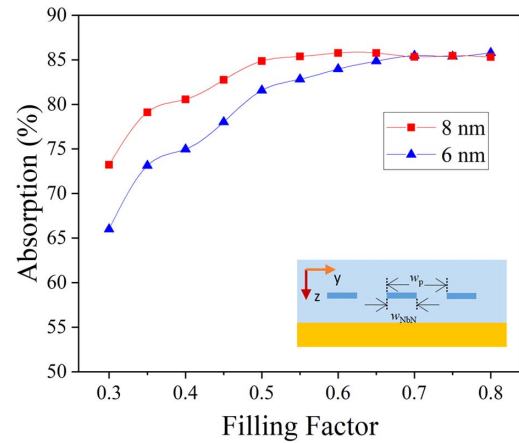


**Fig. 6.** Absorption efficiency as a function of the filling factor. The red squares and blue triangles indicate the absorption of nanowires with 8-nm and 6-nm thickness, with different filling factors, respectively. The inset shows a schematic diagram of the filling factor.

nanowire thickness is 8 nm (red squares), the absorption also tends to increase almost monotonically with an increase in the filling factor. It is worth noting that when the filling factor is lower than 0.5, the absorption curve features a high slope. When the filling factor is larger than 0.5, the absorption curve increases slightly and almost reaches a balance. Therefore, it can be considered that when the filling factor is 0.5, almost all the photons arriving at the focal point are absorbed by the nanowires. However, a higher filling factor implies a longer response time, which will reduce the detection rate; therefore, we consider the filling factor as 0.5 in this study. Figure 6 also shows the situation when the thickness of the nanowire is 6 nm (blue triangles), which is consistent with the above conclusion.

We have theoretically verified the effectiveness of HCG-SNSPD with an example of  $f = 300 \mu\text{m}$ , which affords an appropriate absorption efficiency for 11.5 times the incident area of the nanowires. When designing and optimizing HCG-SNSPDs, we have considered the influence of possible fabrication tolerances on the device performance during its processing, such as the thickness  $d$  of the HCG, the width  $w_g$  of the grating bar, and the deviation of the nanowire position. The influence of these factors on HCG-SNSPD performance will be analyzed below.

Figure 7(a) shows the influence on absorption when the thickness and width of the grating are varied. The thickness  $d$  and width  $w_g$  of the grating discussed here are marked in the inset of Fig. 7(a). Even if the thickness of the grating is reduced to  $0.65 \mu\text{m}$  or increased to  $0.85 \mu\text{m}$ , the absorption can remain above 73%. Moreover, when the ratio of bar width changes between 0.9 and 1.1, the absorption is also above 70%. In other words, if the grating thickness  $d$  and the bar width  $w_g$  vary within  $\pm 0.1 \mu\text{m}$  and  $\pm 10\%$ , respectively, the absorption efficiency of HCG-SNSPD can still be maintained above 70% without a significant drop. It is worth noting that the change of grating thickness and bar width will cause a shift of the HCG-SNSPD's working band. If the thickness or bar width of the grating is increased, the working band will shift to longer wavelengths. Conversely, it will shift to shorter wavelengths. In our

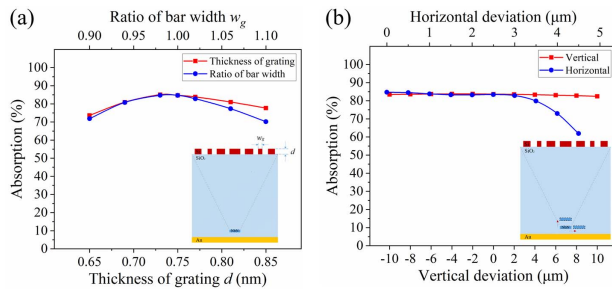


**Fig. 7.** Influence of fabrication tolerances on absorption results (at the wavelength of 1550 nm). (a) Absorption as a function of the thickness  $d$  and the ratio of bar width  $w_g$  of the grating. The inset illustrates the grating parameters represented by  $d$  and  $w_g$  in the structure. (b) Absorption as a function of vertical and horizontal deviations of nanowire positions. The inset shows the vertical and horizontal deviation positions of the nanowires. Due to the symmetry, the horizontal deviation is shown in one direction. The positive and negative values of the vertical deviation represent the downward and upward shifts, respectively.

numerical simulation results, if the grating thickness  $d$  and the bar width  $w_g$  vary within  $\pm 0.1$  μm and  $\pm 10\%$ , respectively, the bandwidth of the high absorption spectrum will shift within  $\pm 40$  nm, and the reduction in absorption efficiency is less than 10%. It can be considered that such variations do not have a significant influence on high absorption and bandwidth.

Besides the grating, the position of the nanowires may be deviated because of the overlay accuracy, which means that they may not be perfectly placed at the center of the focus. We have fully considered this tolerance in the preparation process at the beginning of the design of the structure. The possible horizontal and vertical deviations of the nanowire positions are illustrated in the inset of Fig. 7(b). The deviation here refers to the distance that the center point of the nanowires moves in the horizontal or vertical direction. For the horizontal deviation [blue line in Fig. 7(b)], there is a very small decrease in absorption in the range of 3.5 μm, but the overall remains above 80%. When the deviation is greater than 3.5 μm, the decreasing slope of the absorption starts to increase rapidly. This phenomenon is easy to explain. The width of the focal spot is  $\sim 5$  μm, but the width of the nanowires region we designed is 10 μm, which is twice as large as the size of the focal spot. The overlay accuracy of the lithography system is usually less than 1 μm, which means there is sufficient redundancy to keep the high absorption efficiency of HCG-SNSPD. A similar explanation can be applied for the vertical deviation [red line in Fig. 7(b)]. The focus point is an FWHM  $\sim 50$  μm in the  $z$  direction shown in Fig. 3(a), so the nanowires have a larger allowable range of deviation in the vertical direction. Our numerical calculations show that when the vertical deviation is within a range from  $-10$  μm to 10 μm, the absorption is maintained above 82%. Moreover, the actual allowable tolerance range would be much larger because the line is almost horizontal. In general, although there are certain fabrication tolerances in the grating and the position of nanowires, they basically do not influence the absorption efficiency of HCG-SNSPD, which means the overall structure has high fault tolerance.

## 4. DISCUSSION

We have proved that SNSPD integrated with HCG can achieve high-efficiency broadband detection in the NIR band with a large light-receiving area. Prior to our work, phase gratings and metal-insulator-metal (MIM) circular gratings were integrated into SNSPD to increase its light-receiving area [33,34]. SiO<sub>2</sub> phase gratings are capable of converting incident light. The plane light passing through the phase gratings would form bright and dark stripes with period equal to the grating. The nanowires of SNSPD are usually distributed uniformly, so it can be placed only at the bright stripe position by using the effect of phase gratings, which can reduce the filling factor of nanowires by half and achieve the purpose of increasing the receiving area and detection rate of SNSPD. This approach has some effect, but the enhancement is limited compared to our current work. Since the period of the phase grating is fixed, the nanowires can achieve high absorption only at a certain wavelength, and it cannot achieve high absorption efficiency when the incident light is at a continuous wavelength like HCG-SNSPD. The MIM circular grating is based on surface plasmon polaritons (SPPs). SPPs are electromagnetic excitations existing at the interface between a metal and a dielectric material, which can be utilized to manipulate light at a sub-wavelength scale. Wang *et al.* proposed the MIM circular grating to concentrate incident light and enhance the optical density arriving at SNSPD. Although the MIM circular grating can improve the light density at the SNSPD position, the ring is made of metal, which would cause very high reflection and transmission losses of incident light. In fact, the absorption efficiency of the SNSPD is not increased compared to the total incident light above the grating because most of it is lost during the transmission process. Such a problem does not exist in our work because the Si and SiO<sub>2</sub> in the structure have almost no absorption for light in the NIR band.

In addition to the method of using integrated gratings to achieve large receiving areas for SNSPDs, lenses are also used in SNSPDs to achieve convergence of light. Zhang *et al.* assisted with a dual-lens system to compress beams; a system efficiency of 55% (1550 nm) was achieved for an SNSPD with a detection area of 10 μm × 10 μm and 62.5-μm multimode fiber coupling [32]. It is relatively large in size, because conventional lenses were used, which may occupy limited space in the cryocooler system and consume more cooling resources. Miki *et al.* used small-gradient-index (GRIN) lenses with a diameter of 125 μm to reduce the beam waist of the incident spot in the fiber to 8–10 μm, achieving effective coupling to a 15 μm × 15 μm nanowire area [35]. You *et al.* used GRIN lenses to further compress the spot diameter in the fiber to less than 7 μm, while the GRIN lenses are attached to the fiber in a smaller size [36]. The lenses discussed above are connected to fibers and are not integrated with SNSPD chips, which would limit their application in some scenarios. For example, in applications such as fluorescence microscopy [37], laser-ranging [13], and deep space communication [14], the incident light is usually free-space propagating light. If the incident light needs to be compressed into the fiber before focusing on the nanowire area, it would inevitably incur some losses. Since the HCG-SNSPD is an integrated chip, it can achieve effective coupling

with the incident light not only from the fiber but also from free space.

In the latest study, Xu *et al.* used 3D-printed free-form microlenses to increase the light-receiving area of SNSPD [38]. Its nanowire area is  $4.5 \mu\text{m} \times 4.5 \mu\text{m}$ , and the 3D lens above the nanowire is  $60 \mu\text{m}$  in diameter, which gives SNSPD a 100-fold increase in effective collection area and verifies the effective detection of large-area plane-wave-like free-space illumination. In fact, the rectangular HCG in this work can be designed as a circular HCG with the same parameters [31] to enhance the effective light-receiving area of SNSPD. In other words, if our structure is converted into a circular HCG-SNSPD, the diameter of the theoretically achievable optical reception area would be  $115 \mu\text{m}$ , corresponding to an area of about  $10,387 \mu\text{m}^2$ . In the meantime, the area enhancement factor will exceed 100 times, and the circle can be better coupled with the fiber. However, due to the limited hardware resource condition of our server, we are unable to verify the performance of the complete 3D circular HCG-SNSPD structure with long focus for the time being. Therefore, we have verified the performance of the rectangular HCG-SNSPD in this study and proved the feasibility of our designed structure. Further, both rectangular and circular HCG-SNSPDs can be made into arrays, which would increase the detection area even more and expand the application prospects.

## 5. CONCLUSION

In summary, we theoretically propose a large light-receiving area and high-efficiency SNSPD integrated with HCG. Utilizing the characteristics of high transmittance and phase shift control of HCG, we designed the HCG with a focal length  $f = 300 \mu\text{m}$ , and obtained a high transmittance of 91% in the focal plane, and achieved an appropriate focusing effect. By placing  $10 \mu\text{m} \times 10 \mu\text{m}$  nanowires at the focal point, we integrated the HCG with the SNSPD and obtained 11.5 times the detection area of conventional single-pixel SNSPDs. A high absorption efficiency of 84.9% at a wavelength of 1550 nm is achieved by combining it with the resonant cavity structure. Simultaneously, the HCG-SNSPD achieves an absorption efficiency of more than 70% at wavelengths in the range of 1460 nm to 1650 nm with a high-absorption broadband. Because the area of the nanowires is not expanded while increasing the detection area, the HCG-SNSPD has lower kinetic inductances, which will enable the device to exhibit an improved time performance in practice. Integrating optical structures on devices is a novel approach that will facilitate the design of SNSPDs with a large light-receiving area, high efficiency, and fast response.

**Funding.** China Scholarship Council (201906755016); Natural Science Foundation of Guangdong Province (2018A0303130176, 2019A1515011401); National Natural Science Foundation of China (61801183).

**Disclosures.** The authors declare no conflicts of interest.

**Data Availability.** Data underlying the results presented in this paper are not publicly available at this time but may be obtained from the authors upon reasonable request.

## REFERENCES

- G. N. Gol'tsman, O. Okunev, G. Chulkova, A. Lipatov, A. Semenov, K. Smirnov, B. Voronov, A. Dzardanov, C. Williams, and R. Sobolewski, "Picosecond superconducting single-photon optical detector," *Appl. Phys. Lett.* **79**, 705–707 (2001).
- C. M. Natarajan, M. G. Tanner, and R. H. Hadfield, "Superconducting nanowire single-photon detectors: physics and applications," *Supercond. Sci. Technol.* **25**, 063001 (2012).
- I. Holzman and Y. Ivry, "Superconducting nanowires for single-photon detection: progress, challenges, and opportunities," *Adv. Quantum Technol.* **2**, 1800058 (2019).
- D. Li and R. Jiao, "Design of a low-filling-factor and polarization-sensitive superconducting nanowire single photon detector with high detection efficiency," *Photon. Res.* **7**, 847–852 (2019).
- P. Hu, Y. Ma, H. Li, Z. Liu, H. Yu, J. Quan, Y. Xiao, L. You, Y. Liu, J. Liang, and Z. Wang, "Superconducting single-photon detector with a system efficiency of 93% operated in a 2.4 K space-application-compatible cryocooler," *Supercond. Sci. Technol.* **34**, 07LT01 (2021).
- D. V. Reddy, R. R. Nerem, S. W. Nam, R. P. Mirin, and V. B. Verma, "Superconducting nanowire single-photon detectors with 98% system detection efficiency at 1550 nm," *Optica* **7**, 1649–1653 (2020).
- H. Li, Y. Wang, L. You, H. Wang, H. Zhou, P. Hu, W. Zhang, X. Liu, X. Yang, L. Zhang, Z. Wang, and X. Xie, "Supercontinuum single-photon detector using multilayer superconducting nanowires," *Photon. Res.* **7**, 1425–1431 (2019).
- H. Shibata, K. Shimizu, H. Takesue, and Y. Tokura, "Ultimate low system dark-count rate for superconducting nanowire single-photon detector," *Opt. Lett.* **40**, 3428–3431 (2015).
- A. Vetter, S. Ferrari, P. Rath, R. Alaee, O. Kahl, V. Kovalyuk, S. Diewald, G. N. Goltsman, A. Korneev, C. Rockstuhl, and W. H. P. Pernice, "Cavity-enhanced and ultrafast superconducting single-photon detectors," *Nano Lett.* **16**, 7085–7092 (2016).
- B. Korzh, Q. Zhao, J. P. Allmaras, S. Frasca, T. M. Autry, E. A. Bersin, A. D. Beyer, R. M. Briggs, B. Bumble, M. Colangelo, G. M. Crouch, A. E. Dane, T. Gerrits, A. E. Lita, F. Marsili, G. Moody, C. Peña, E. Ramirez, J. D. Rezac, N. Sinclair, M. J. Stevens, A. E. Velasco, V. B. Verma, E. E. Wollman, S. Xie, D. Zhu, P. D. Hale, M. Spiropulu, K. L. Silverman, R. P. Mirin, S. W. Nam, A. G. Kozorezov, M. D. Shaw, and K. K. Berggren, "Demonstration of sub-3 ps temporal resolution with a superconducting nanowire single-photon detector," *Nat. Photonics* **14**, 250–255 (2020).
- K. Takemoto, Y. Nambu, T. Miyazawa, Y. Sakuma, T. Yamamoto, S. Yorozu, and Y. Arakawa, "Quantum key distribution over 120 km using ultrahigh purity single-photon source and superconducting single-photon detectors," *Sci. Rep.* **5**, 14383 (2015).
- H. Li, L. Zhang, L. You, X. Yang, W. Zhang, X. Liu, S. Chen, Z. Wang, and X. Xie, "Large-sensitive-area superconducting nanowire single-photon detector at 850 nm with high detection efficiency," *Opt. Express* **23**, 17301–17308 (2015).
- L. Xue, M. Li, L. Zhang, D. Zhai, Z. Li, L. Kang, Y. Li, H. Fu, M. Ming, S. Zhang, X. Tao, Y. Xiong, and P. Wu, "Long-range laser ranging using superconducting nanowire single-photon detectors," *Chin. Opt. Lett.* **14**, 071201 (2016).
- M. E. Grein, A. J. Kerman, E. A. Dauler, O. Shatrovov, R. J. Molnar, D. Rosenberg, J. Yoon, C. E. DeVoe, D. V. Murphy, B. S. Robinson, and D. M. Boroson, "Design of a ground-based optical receiver for the lunar laser communications demonstration," in *International Conference on Space Optical Systems and Applications (ICSOS)* (2011), pp. 78–82.
- H. Ivanov, E. Leitgeb, P. Pezzei, and G. Freiberger, "Experimental characterization of SNSPD receiver technology for deep space FSO under laboratory testbed conditions," *Optik* **195**, 163101 (2019).
- X. Li, J. Tan, K. Zheng, L. Zhang, L. Zhang, W. He, P. Huang, H. Li, B. Zhang, Q. Chen, R. Ge, S. Guo, T. Huang, X. Jia, Q. Zhao, X. Tu, L. Kang, J. Chen, and P. Wu, "Enhanced photon communication through Bayesian estimation with an SNSPD array," *Photon. Res.* **8**, 637–641 (2020).

17. S. Chen, D. Liu, W. Zhang, L. You, Y. He, W. Zhang, X. Yang, G. Wu, M. Ren, H. Zeng, Z. Wang, X. Xie, and M. Jiang, "Time-of-flight laser ranging and imaging at 1550 nm using low-jitter superconducting nanowire single-photon detection system," *Appl. Opt.* **52**, 3241–3245 (2013).
18. S. Steinhauer, S. Gyger, and V. Zwiller, "Progress on large-scale superconducting nanowire single-photon detectors," *Appl. Phys. Lett.* **118**, 100501 (2021).
19. H. Hemmati, A. Biswas, and I. B. Djordjevic, "Deep-space optical communications: future perspectives and applications," *Proc. IEEE* **99**, 2020–2039 (2011).
20. C. Yu, J. Qiu, H. Xia, X. Dou, J. Zhang, and J. Pan, "Compact and lightweight 1.5  $\mu\text{m}$  lidar with a multi-mode fiber coupling free-running InGaAs/InP single-photon detector," *Rev. Sci. Instrum.* **89**, 103106 (2018).
21. C. L. Lv, H. Zhou, H. Li, L. X. You, X. Y. Liu, Y. Wang, W. J. Zhang, S. J. Chen, Z. Wang, and X. M. Xie, "Large active area superconducting single-nanowire photon detector with a 100  $\mu\text{m}$  diameter," *Supercond. Sci. Technol.* **30**, 115018 (2017).
22. Q. Chen, B. Zhang, L. Zhang, R. Ge, R. Xu, Y. Wu, X. Tu, X. Jia, D. Pan, L. Kang, J. Chen, and P. Wu, "Sixteen-pixel NbN nanowire single photon detector coupled with 300- $\mu\text{m}$  fiber," *IEEE Photon. J.* **12**, 6800112 (2020).
23. J. P. Allmaras, A. D. Beyer, R. M. Briggs, F. Marsili, M. D. Shaw, G. V. Resta, J. A. Stern, V. B. Verma, R. P. Mirin, S. W. Nam, and W. H. Farr, "Large-area 64-pixel array of WSi superconducting nanowire single photon detectors," in *Conference on Lasers and Electro-Optics (CLEO)* (2017), pp. 1–2.
24. M. Yabuno, S. Miyajima, S. Miki, and H. Terai, "Scalable implementation of a superconducting nanowire single-photon detector array with a superconducting digital signal processor," *Opt. Express* **28**, 12047–12057 (2020).
25. C. J. Chang-Hasnain and W. Yang, "High-contrast gratings for integrated optoelectronics," *Adv. Opt. Photon.* **4**, 379–440 (2012).
26. D. Fattal, J. Li, Z. Peng, M. Fiorentino, and R. G. Beausoleil, "Flat dielectric grating reflectors with focusing abilities," *Nat. Photonics* **4**, 466–470 (2010).
27. F. Lu, F. G. Sedgwick, V. Karagodsky, C. Chase, and C. J. Chang-Hasnain, "Planar high-numerical-aperture low-loss focusing reflectors and lenses using subwavelength high contrast gratings," *Opt. Express* **18**, 12606–12614 (2010).
28. W. Fang, Y. Huang, J. Fei, X. Duan, K. Liu, and X. Ren, "Concentric circular focusing reflector realized using high index contrast gratings," *Opt. Commun.* **402**, 572–576 (2017).
29. T. Shiono, M. Kitagawa, K. Setsune, and T. Mitsuyu, "Reflection micro-Fresnel lenses and their use in an integrated focus sensor," *Appl. Opt.* **28**, 3434–3442 (1989).
30. L. Redaelli, G. Bulgarini, S. Dobrovolskiy, S. N. Dorenbos, V. Zwiller, E. Monroy, and J. M. Gérard, "Design of broadband high-efficiency superconducting-nanowire single photon detectors," *Supercond. Sci. Technol.* **29**, 065016 (2016).
31. C. Ma, Y. Huang, and X. Ren, "High-numerical-aperture high-reflectivity focusing reflectors using concentric circular high-contrast gratings," *Appl. Opt.* **54**, 973–978 (2015).
32. L. Zhang, C. Wan, M. Gu, R. Xu, S. Zhang, L. Kang, J. Chen, and P. Wu, "Dual-lens beam compression for optical coupling in superconducting nanowire single-photon detectors," *Sci. Bull.* **60**, 1434–1438 (2015).
33. M. Gu, L. Kang, L. Zhang, Q. Zhao, T. Jia, C. Wan, R. Xu, X. Yang, and P. Wu, "A high-efficiency broadband superconducting nanowire single-photon detector with a composite optical structure," *Chin. Phys. Lett.* **32**, 038501 (2015).
34. S. Wang, F. Chen, Y. Zhang, Q. Li, X. Sun, X. Chen, and W. Lu, "Simulation of superconducting single photon detector coupled with metal-insulator-metal circular grating," in *13th International Conference on Numerical Simulation of Optoelectronic Devices (NUSOD)* (2013), pp. 131–132.
35. S. Miki, T. Yamashita, M. Fujiwara, M. Sasaki, and Z. Wang, "Multichannel SNSPD system with high detection efficiency at telecommunication wavelength," *Opt. Lett.* **35**, 2133–2135 (2010).
36. L. You, J. Quan, Y. Wang, Y. Ma, X. Yang, Y. Liu, H. Li, J. Li, J. Wang, J. Liang, Z. Wang, and X. Xie, "Superconducting nanowire single photon detection system for space applications," *Opt. Express* **26**, 2965–2971 (2018).
37. J. Yu, R. Zhang, Y. Gao, Z. Sheng, M. Gu, Q. Sun, J. Liao, T. Wu, Z. Lin, P. Wu, L. Kang, H. Li, L. Zhang, and W. Zheng, "Intravital confocal fluorescence lifetime imaging microscopy in the second near-infrared window," *Opt. Lett.* **45**, 3305–3308 (2020).
38. Y. Xu, A. Kuzmin, E. Knehr, M. Blaicher, K. Ilin, P.-I. Dietrich, W. Freude, M. Siegel, and C. Koos, "Superconducting nanowire single-photon detector with 3D-printed free-form microlenses," *Opt. Express* **29**, 27708–27731 (2021).